

Article

Influence of Tip Clearance on Flow Characteristics of Axial Compressor

Moru Song , Hong Xie, Bo Yang * and Shuyi Zhang

School of Mechanical Engineering, Shanghai Jiao Tong University, Shanghai 200240, China;
samuel0624@sjtu.edu.cn (M.S.); xiehong1211@sjtu.edu.cn (H.X.); shuyizhang@sjtu.edu.cn (S.Z.)

* Correspondence: byang0626@sjtu.edu.cn; Tel.: +86-21-3420-6871

Received: 9 September 2020; Accepted: 10 November 2020; Published: 11 November 2020



Abstract: This paper studies the influence of tip clearance on the flow characteristics related to the performance. Based on full-passage numerical simulation with experimental validation, several clearance models are established and the performance curves are obtained. It is found that there exists an optimum clearance for the stable working range. By analyzing the flow field in tip region, the role of the tip leakage flow is illustrated. In the zero-clearance model, the separation and blockage along the suction side is the main reason for rotating stall. As the tip clearance is increased to the optimum value, the separation is suppressed by the tip leakage flow. However, with the continuing increasing of the tip clearance, the scale and strength of the tip clearance vortex is increased correspondingly. When the tip clearance is larger than the optimum value, the tip clearance vortex gradually dominates the flow field in the tip region, which can increase the unsteadiness in the tip region and trigger forward spillage in stall onset.

Keywords: axial compressor; tip clearance; flow field; numerical simulation

1. Introduction

It is the tip region of a rotor that is one of the most unstable regions in an axial compressor. For example, for the tip-critical rotors, the rotating stall was first observed in the tip region. In the tip region, there exists the maximum rotating linear velocity, tip leakage flow, and boundary layer flow, etc. Among these flows, the tip leakage flow, induced by the pressure difference between blade sides, plays the most important role on the flow behavior. The tip leakage flow is closely related to the tip clearance, which is one of the key parameters for the design and manufacture of an axial compressor. As the tip clearance is changed, not only is the strength of the leakage flow changed, but also other flow structure and distribution are influenced greatly, especially under a near-stall condition. Therefore, the performance and stable working range is varied with the tip clearance.

In the last century, many researches focused on the influence of tip clearance in an overall manner. Combined experiment data with potential-vortex model, Lakshminarayana [1] proposed a formula, firstly, to evaluate the stage efficiency in different tip clearance. Based on this formula, the pressure ratio and efficiency can be improved by the reduction of the tip clearance. Inoue et al. [2,3] obtained and described the roll-up tip clearance vortex(TCV) by hotwire. From the vortex model, the flows in the tip region could be divided into the main flow region and tip leakage flow region. Day [4] also proposed the influence of the tip clearance on off-design conditions in axial compressors.

As the experiment method and computational fluid dynamic method have been both highly improved, the flow structures and special phenomenon in the tip region were studied in detail, which included double leakage, vortex breakdown, self-induced flow, and active control technology, etc. For double leakage, it was first noticed by Khalsa et al. [5] in the experiment and simulation results. They pointed out that the relative stagnation pressure is decreased by double leakage; therefore, the loss

and blockage were increased. Double leakage flow was much influenced by clearance size, working condition, and unsteady interaction from the stator, which was illustrated by Mailach et al. [6,7], Sirakov et al. [8], and Du et al. [9]. By the means of Large-eddy simulation (LES) approach, Hah [10] studied the double leakage flow under the large tip clearance model. As double leakage flow occurred in all working conditions with large tip clearance, vortex rope is generated near leading edge, which results in the high mixing loss and non-synchronous vibration.

For the breakdown of tip clearance vortex, Lotzerich [11] and Furukawa et al. [12] both noticed this phenomenon at almost the same time. Later, Furukawa et al. [13,14] summarized the characteristics by the means of experiment and computational fluid dynamics (CFD). When the vortex breakdown occurs, the disappearance of vortex core and the roll-up structure causes the large low-velocity cells. The vortex breakdown always occurred in near-stall condition, because the adverse pressure gradient and the unsteadiness reached the maximum values in the tip region. Yamada et al. [15] presented the unsteady flowing field near the tip region by the CFD method with a single passage grid. It is shown that the TCV is broken down by the effect of the shock wave, and the type of vortex breakdown in near-peak point was different with its in near-stall condition.

From the research above, it is understood that, under near-stall condition, the tip clearance vortex will be highly unsteady and unstable. Therefore, the stall inception was always detected in the tip region. Using a hotwire arranged around the rotor tip of the axial compressor, circumferentially, McDougall et al. [16,17] captured the large propagating wave with small amplitude in near-stall condition, which is called a modal type rotating stall. Later, Day et al. [4,18] captured the short propagating wave with large amplitude, which was a spike type rotating stall. Hoying et al. [19] studied the relation between the rotating stall and tip clearance vortex in the E3 compressor. By using Reynolds averaged Naiver-Stokes simulation (RANS) method, it was found that the tip clearance vortex will move forward to rotor inlet in near-stall condition. Hah et al. [20] and Vo et al. [21] proposed the criterion for the spike initiated rotating stall, which had leading edge spillage and trailing edge backflow. This criterion was already accepted by many researchers. However, many people misunderstood this criterion and considered the tip clearance vortex as the origin of the rotating stall.

By means of unsteady multi-passage simulation, Pullan et al. [22] illustrated two different stall mechanisms. It was pointed out that the stall originated from high incidence of the rotor inlet. Although tip clearance was not necessary for the rotating stall, it does influence the stall characteristics a lot. Later, Smith et al. [23] illustrated the influence of tip clearance on the rotating stall. There existed an optimum tip clearance for stall margin, which can balance the effect from the different stall mechanisms.

However, in their works, the stall was triggered by several re-staggered blades. It was more appropriate to use the non-re-staggered blade model. Although they studied the relationship between stall and tip clearance, they focused on the stall mechanism in the zero clearance model, the evolution of stall mechanism and the effect of the tip clearance vortex in different clearances were not analyzed enough. In addition, the benefit of leakage flow was not mentioned.

This paper studies the influence of tip clearance on flow characteristics related to performance. Based on the full-passages model, steady and unsteady results are obtained by the RANS method. The relationship between the stability of the compressor and the tip clearance is discussed. Then, the flowfield characteristics under different tip clearances are compared, and the effects of the separation and the tip leakage flow on the efficiency and stability are discussed.

2. Experiment and Numerical Setup

2.1. Description of the Test Rig and the Measurement

The test was conducted in the 1–1/2 stage axial subsonic compressor in Shanghai Jiao Tong University. The blade number of inlet guide vane (IGV) is 32, and 29 and 37 for rotor and stator, respectively. The hub-tip ratio is 0.76. The design rotating speed is 17,000 rpm. Since this research is

focused on the subsonic conditions, the rotational speed is adopted as 12,000 rpm, so that the tip Mach number is less than 0.9. The design tip clearance is 98.7% of span.

Compressor performance is obtained by the adjusting of the throttle area behind the stator. A flowmeter is equipped at the upstream of IGV to obtain flow rate. Total pressure is measured by two five-hole total pressure probes mounted at upstream and downstream of the compressor, respectively. Temperature probes are also used at both upstream and downstream to estimate isentropic efficiency.

The overall performance parameters are defined by the following equations.

$$\eta = \frac{H_{i,out} - H_{in}}{H_{out} - H_{in}} \quad (1)$$

$$\pi = \frac{p_{t,out}}{p_{t,in}} \quad (2)$$

$$\xi = \frac{\dot{m}_{in}/\pi}{\dot{m}_{in,DP}/\pi_{DP}} \quad (3)$$

where η is isentropic efficiency, $H_{i,out}$ isentropic outlet enthalpy, H_{in} inlet enthalpy, H_{out} outlet enthalpy, π total pressure ratio, $p_{t,out}$ isentropic outlet total pressure, $p_{t,in}$ inlet total pressure, ξ flow rate coefficient, \dot{m}_{in} mass flow rate, $\dot{m}_{in,DP}$ mass flow rate at design point, and π_{DP} total pressure ratio at design point.

2.2. Numerical Model

The numerical simulation is accomplished by using a commercial CFD code, NUMECA. It is a popular solver for the flowfield simulation of turbomachinery. With the features of structured-grid supported, the finite-volume method and the suitable numerical treatments, the three-dimensional (3D) steady and unsteady flowfield can be obtained for the axial compressor.

The calculation area is between Section A and Section B in Figure 1. The upstream channel and downstream channel are extended as much as two IGV blade chord lengths and three stator blade chord lengths, respectively. Five cases with different tip clearance sizes from 0% to 2% of chord length are established and marked as 0%, 0.5%, 1%, 1.5%, and 2% of the chord length of blade tip τ , respectively.

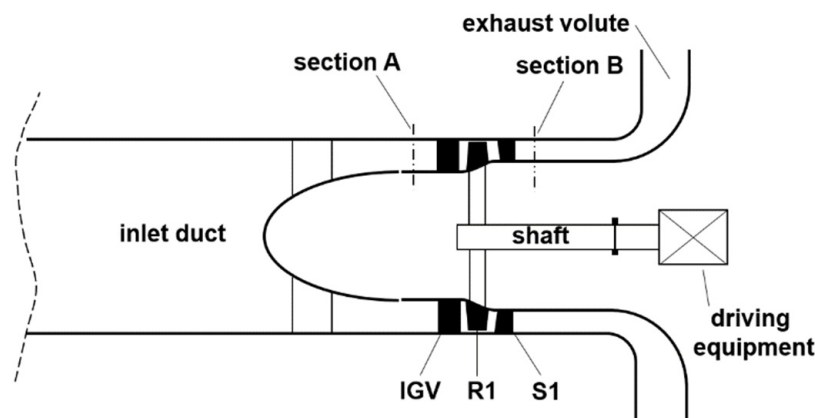


Figure 1. Sketch of the test rig.

Real air model is adopted as working fluid. The two-order central difference spatial scheme of Jameson is adopted in this study. Spalart–Allmaras (SA) model by Spalart et al. [24], which is widely applied in industry and academia, is also used in this study. For the inlet condition, total pressure, total temperature, and the velocity direction are specified, and refer to the experiment data. For the outlet condition, the static pressure is applied with the radial equilibrium. The rotating speed is applied on the rotor passage, while the other passages keep station. When processing the steady simulation, the mixing plane method is used to transfer the flowfield information between rotating

region and station region. Multigrid and local time stepping treatment are also applied to accelerate the calculation. The steady simulation is considered as converged when the mass flow is balanced and all of the residual lines are stable or fluctuate periodically. With the increasing of the outlet pressure, the last converged steady simulation is considered as near-stall (NS) condition. The unsteady method for this model had been discussed by Song et al. [25], including using the dual time step method of Jameson [26] and the sliding mesh method [27]. The 20 timesteps are set in every rotor passing period, and the number of the inner iteration step is set to 50. When the periodic fluctuation of the mass flow and the static pressure on the numerical probes is continued for ten passing times, it is considered as converged for the unsteady simulation.

2.3. Grid Generation and Independent Test

O4H-type topology is adopted in every row. The y^+ is less than 5 to ensure capturing the blade loading more accurately. Mesh in tip clearance is refined to 17 layers in radial direction. Three sets of grids are generated to validate the grid independence. The grid number of every passage is shown in Table 1. From validation results shown in Figure 2, grid2 is appropriate for the calculation. A three level multi-grid is adopted to accelerate the calculation. The chosen grid is shown in Figure 3. In order to transfer the flow information between stational region and rotational region, the mixing plane method is used in this simulation.

Table 1. Grid number of three sets of grids ($\times 10^6$).

Mesh	Inlet Guide Vane (IGV)	Rotor	Stator	Full-Passages
Grid1	0.34	0.31	0.38	33.55
Grid2	0.53	0.64	0.58	56.40
Grid3	0.64	0.79	0.71	68.95

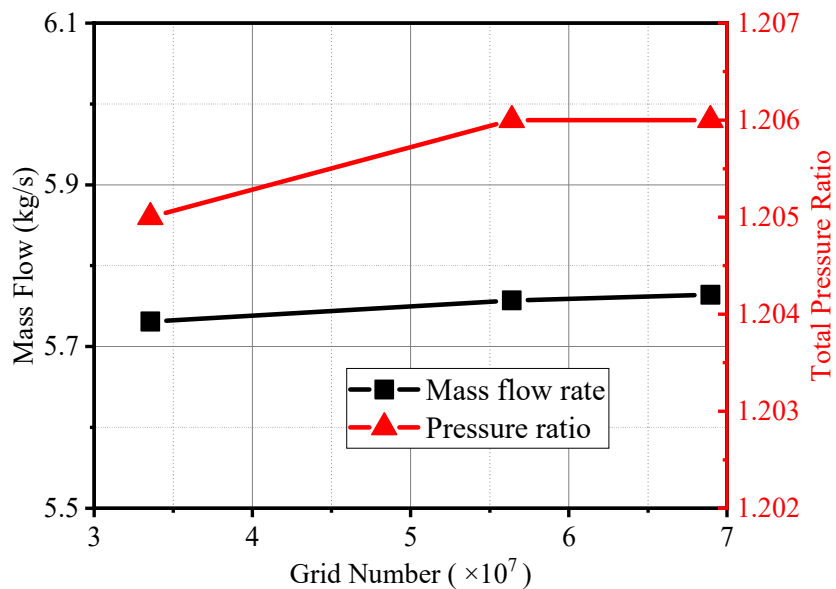


Figure 2. Validation for grid independence.

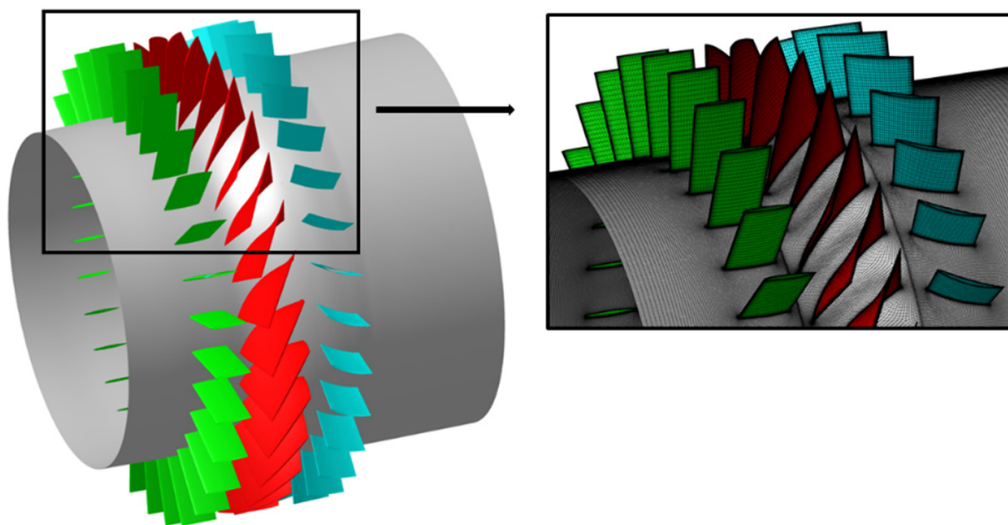


Figure 3. One passage of grid for simulation.

2.4. Model Validation

Based on the chosen grid, the performance curve is obtained by the numerical simulation. From Figure 4, by using the full-wheel simulation, the simulated mass flow range is enlarged and the numerical result is closer to the experiment data. It is found that the numerical results are always larger than experiment data; this might be the result of the neglection of the blade hub fillet in the numerical model. Even so, the numerical results match well with the experiment data on most mass flow conditions.

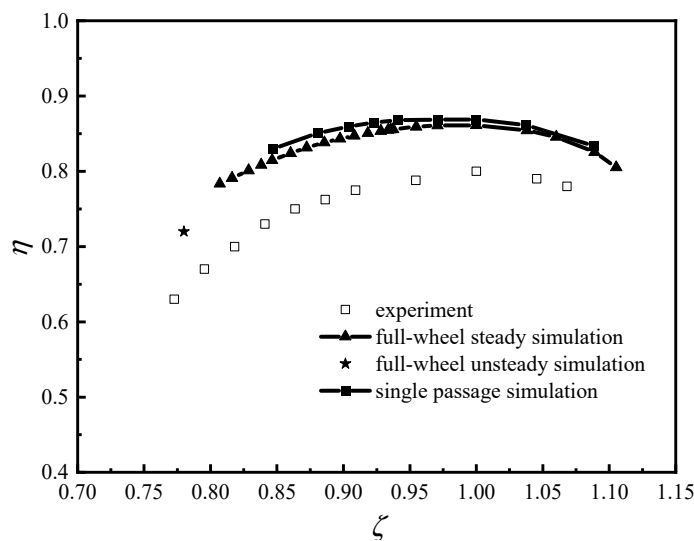


Figure 4. Performance comparison between experimental and numerical results.

3. Results

In this section, the influence of tip clearance on the performance is studied. The trend of performance change is discussed with the clearance increased from zero ($0\% \tau$) to large ($2\% \tau$), and the characteristics under peak efficiency (PE) working point and near stall (NS) working point are compared and discussed.

3.1. Overall Performance

Performance curves of every clearance model are shown in Figure 5. In a mass, the efficiency and pressure ratio are decreased as clearance size is increased, which is coherent with conclusions from predecessors' work. However, there is a certain tip clearance size, so that the stable working range can reaches to the maximum, which can be observed from stall margin change (Figure 6). The maximum surge margin is found in the design clearance model. When the tip clearance is larger or less than the design clearance model, the stall margin is decreased, obviously. In other words, with the tip leakage flow, the stability of the compressor might be enhanced. So, it is meaningful to find out the mechanism of leakage flow that turns the negative influence to positive influence on stall margin.

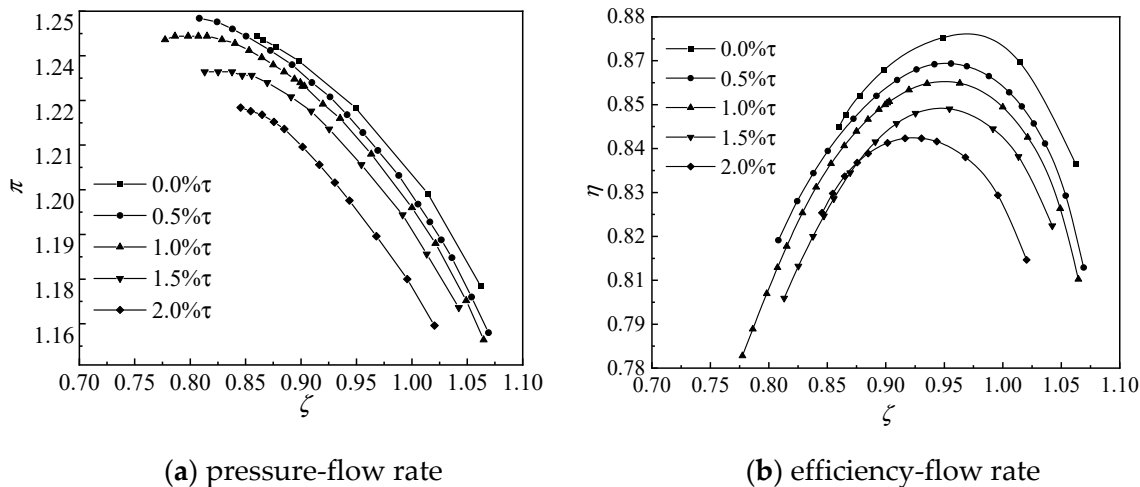


Figure 5. Performance curves of different tip clearance models. (a) pressure-flow rate; (b) efficiency-flow rate.

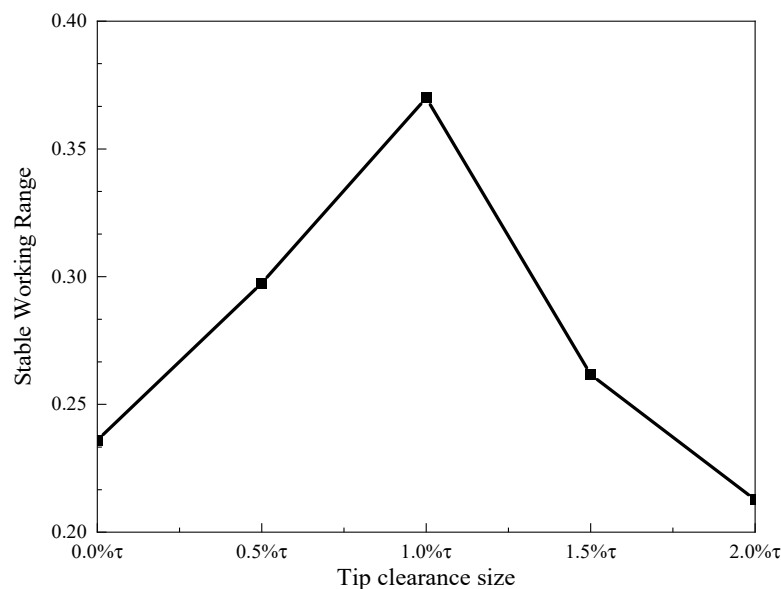


Figure 6. Stable working range under different clearance models.

The rotor loss factors along span is shown in Figure 7. The dimensionless rotor loss factor is defined in Equation (4).

$$F_r = \frac{P_{i,t,r} - P_{o,t,r}}{P_{i,d,r} - P_{o,d,r}} \quad (4)$$

where P is the pressure, subscript i, o, t, d , and r represent the rotor inlet, outlet, total, dynamic quantities and relative quantities, respectively. Along the span, the loss in tip region is the maximum. With the increasing of tip clearance, the loss in tip region is increased correspondingly. In addition, in tip region, loss factor is increased rapidly from $0\%\tau$ to $1\%\tau$, which illustrates the negative impact of tip leakage on efficiency. When the tip clearance is over $1\%\tau$, loss in tip region is stable with the increasing of tip clearance.

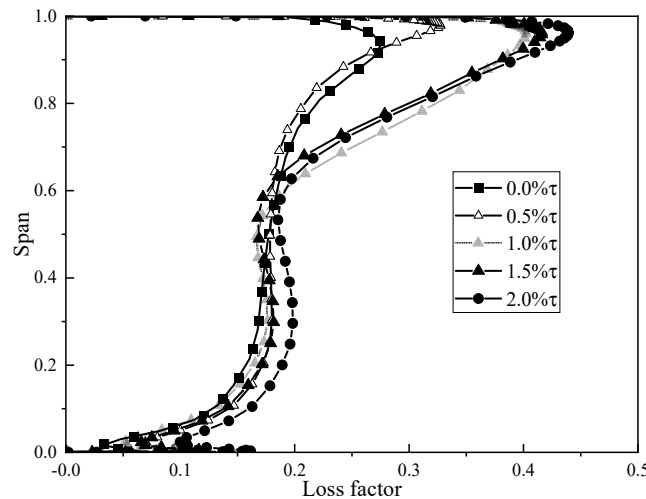


Figure 7. Loss factor distribution under different clearance models.

Figure 8 shows the blade loading at 98% of span. Pressure coefficient is defined in Equation (5):

$$CP = \frac{P_{s,o} - P_{s,i}}{P_{s,i}} \quad (5)$$

where subscript s represents the static quantities. The blade loading of zero-clearance model is over two times larger than that of design-clearance. As the tip clearance is increased, the blade loading is decreased, which is benefit for the safety of the blade. This can be explained that the tip leakage flow can balance the pressure difference between the pressure side (PS) and the suction side (SS).

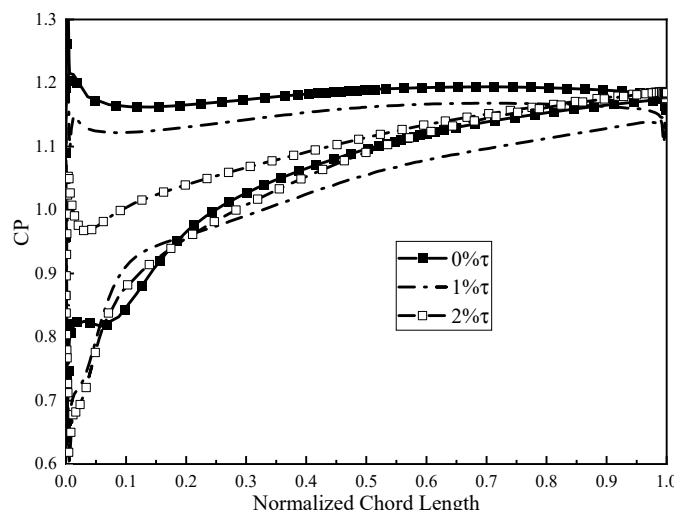


Figure 8. Pressure coefficient distribution at blade tip under different clearance models.

3.2. Detail Results of Zero Clearance Model

In this model, there is no tip leakage flow or tip clearance vortex at all. At 96% of span, relative Mach number contours with streamline of relative velocity are presented in Figure 9a. Under PE condition, there is seldom low-Mach region, except the boundary layer on the blade surface. From the streamline, since the incidence angle matches with the stagger angle, the flowfield is well without any vortex or separation. Under NS condition, there is a large area of the blockage region from the LE to the neighboring LE, and from the SS to PS. Since the mass flow is decreased, the incidence angle is far from the blade stagger angle, so a vortex is generated near the PS close to LE, and enrolls the surrounding fluid, with which the leading-edge spillage is occurred.

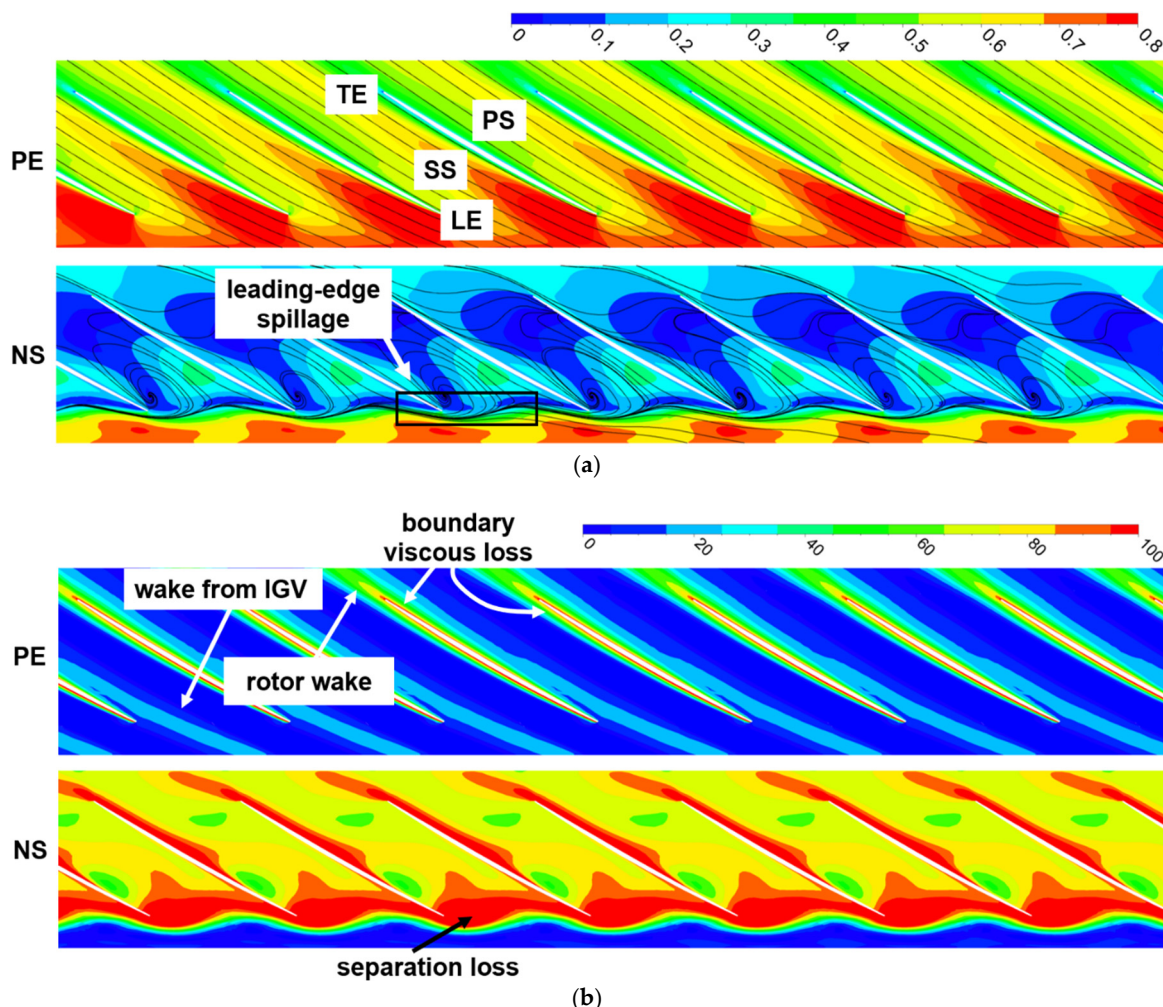


Figure 9. Time-averaged results at 96% of span. (a): Relative Mach contours with streamline of relative velocity. (b): Entropy contours ($\text{J}/(\text{kg K})$).

Static entropy contour is often used to illustrate the loss distribution. Moreover, it is often used at tip span to locate the boundary of the tip leakage flow and the separation flow, because high loss will be induced when circumferential tip leakage flow/separation flow and main flow are interacted, in which the vortex would be generated and developed, and by which the entropy gradient is largest among tip-span contour. Static entropy contours are shown in Figure 9b. Under PE condition, the loss in the tip region consists of the wake loss from IGV, the boundary viscous loss and the wake from the rotor blade. The loss area and the amplitude are both low. Under the NS condition, it is found that the high-gradient interface is shifted forwardly to the front of the LE, which is coherent with the LE spillage from Figure 9a. Compared with the figure of PE, the loss region and the amplitude are

highly increased. The separation loss occupies the whole passage inlet, by which the loss on the whole passage, especially on the pressure, is highly increased.

In order to observe 3D distribution of separation and blockage, streamlines in the tip region are drawn in Figure 10 with velocity flux contours at passage cutting planes. The blockage area is attached to the casing-suction corner and reduced with the decreasing of radial distance. Along the suction side surface, streamline flows toward the tip region. When the flow arrives to casing, it turns to the middle passage along the casing side, and finally flows to the downstream due to the mixing process with the main flow. From the 3D streamline in Figure 10a, and limiting streamline in Figure 10b, the separation and blockage along the suction side is caused by leading-edge separation and the corner separation.

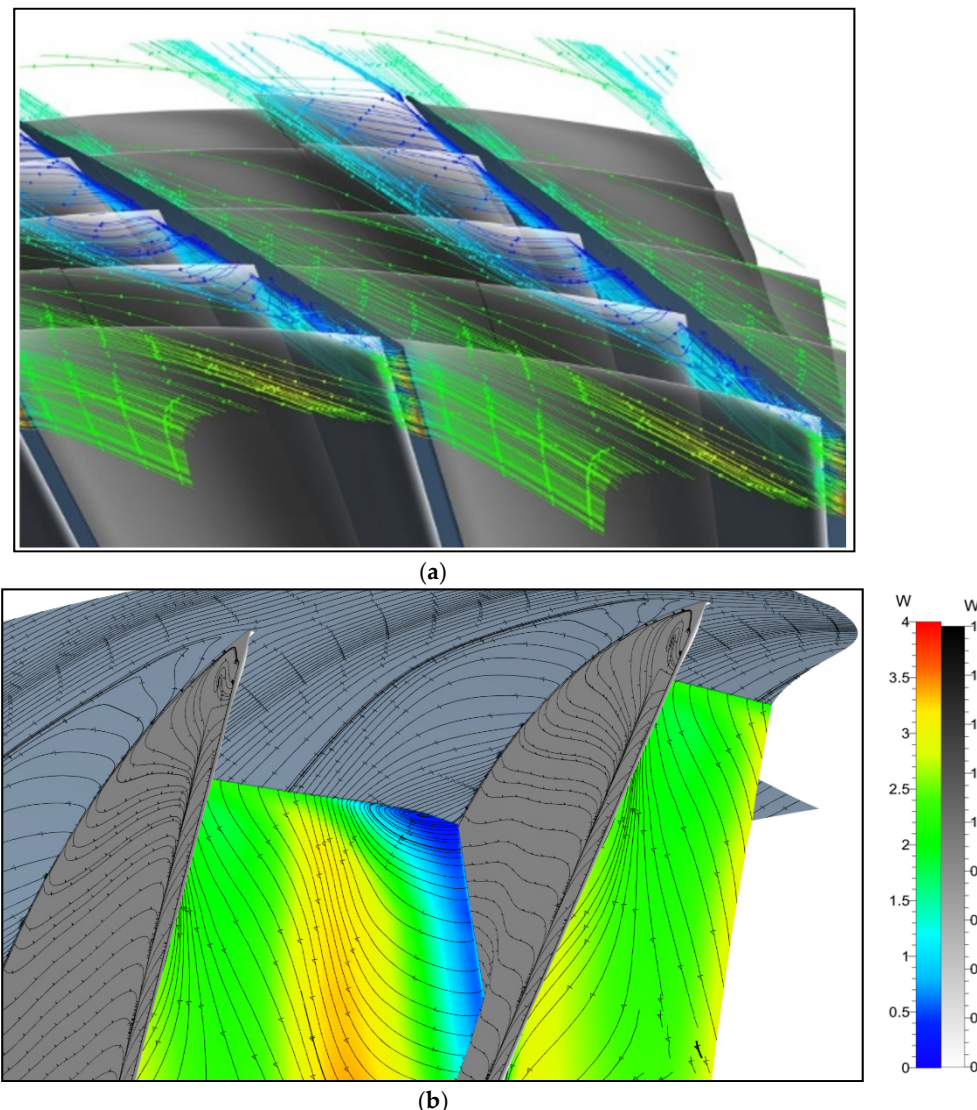


Figure 10. The three-dimensional (3D) figures for the passage flowfield. (a): streamlines in tip region with velocity flux contours at passage cutting planes. (b): streamlines in tip region with velocity flux contours at passage cutting planes.

For PE and NS conditions, here are the iso-surfaces of vorticity at $\nu = 0.25$ in Figure 11. ν is defined as follows.

$$\nu = \frac{\Omega^2 + S^2}{\omega^2} \quad (6)$$

where Ω , S , ω are the symmetric and antisymmetric parts of the gradient velocity tensor. Since the flow is very steady, only the steady result is shown for the PE condition.

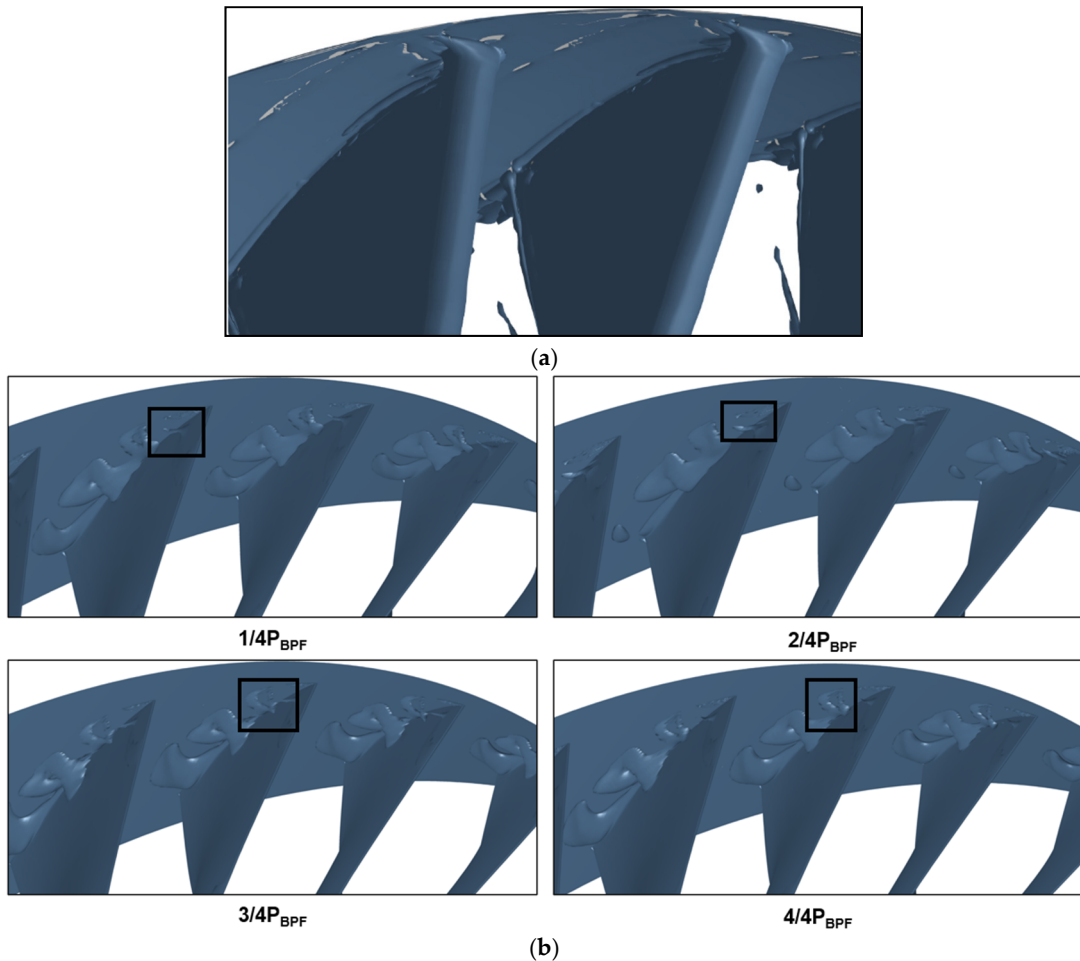


Figure 11. Iso-surfaces of instantaneous vorticity at $\lambda = 0.25$. (a): Peak efficiency (PE), steady results. (b): Near-stall (NS), transient result, P_{BPF} is the period of the blade passing.

It is different between the vortex distribution in PE and NS condition. For PE condition, there is no large vorticity cell in flow passage. However, there are two parts that are worthy to pay attention to. In the front and rear part of suction side, some little vorticity cells attach to the corner, from which the effect of corner separation is illustrated. In addition, vorticity cells in front of LE develop in a circumferential direction, which is the result of the effect of LE separation and casing separation. When the condition reaches to NS, from the black box in Figure 11b, these vorticity cells grow up to large cells, and shed with the period of blade passing. Flow incidence in front of the rotor passage will be increased because of the blockage, which will cause larger separation and corresponding larger blockage in the next passage. When the flow incidence increases to extent, leading edge spillage will occur, as shown in Figure 9a.

In Figure 12, the axial component of the velocity is shown in order to illustrate the unsteadiness of the velocity under NS condition. Although there is the vortex generation and moving by the leading-edge separation and corner flow, the unsteadiness is still very low. From the $\frac{1}{4}$ of the period of the blade passing (P_{BPF}) to $4/4 P_{BPF}$, there is seldom unsteadiness that can be observed. This is because the blockage decreases the amplitude of the unsteadiness. In order to qualify the unsteadiness in NS condition, we set static pressure probes in front of LE, and the spectrum result is shown in Figure 13.

The spectrum is dominated by character frequency related to rotation, including rotation frequency and blade passage frequency.

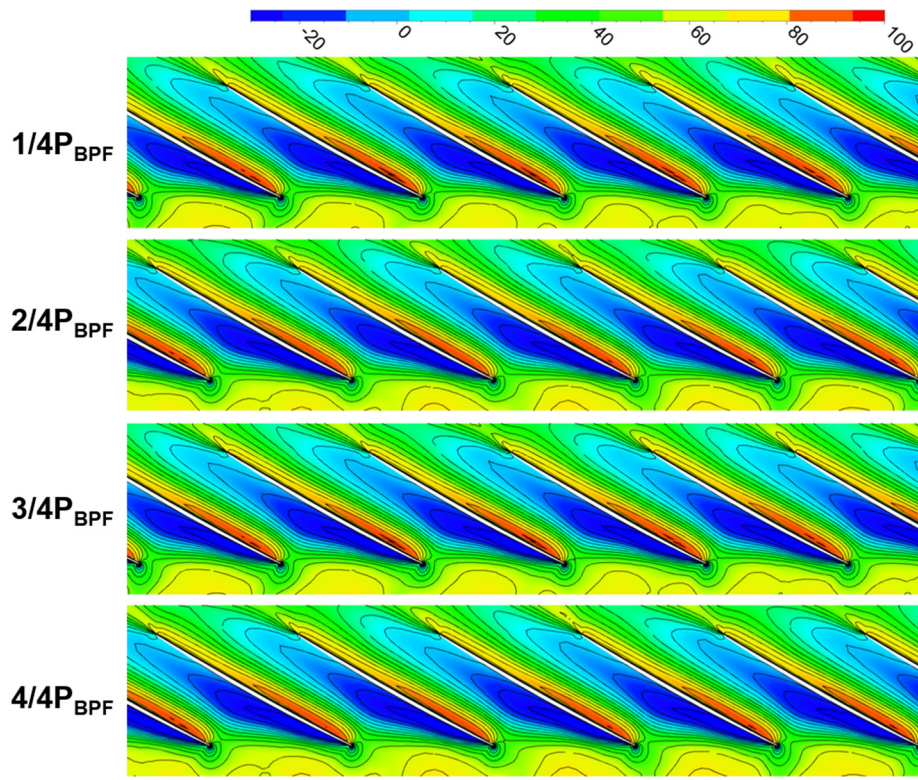


Figure 12. Axial component of velocity under NS condition, 99.35% of span, P_{BPF} is the period of the blade passing.

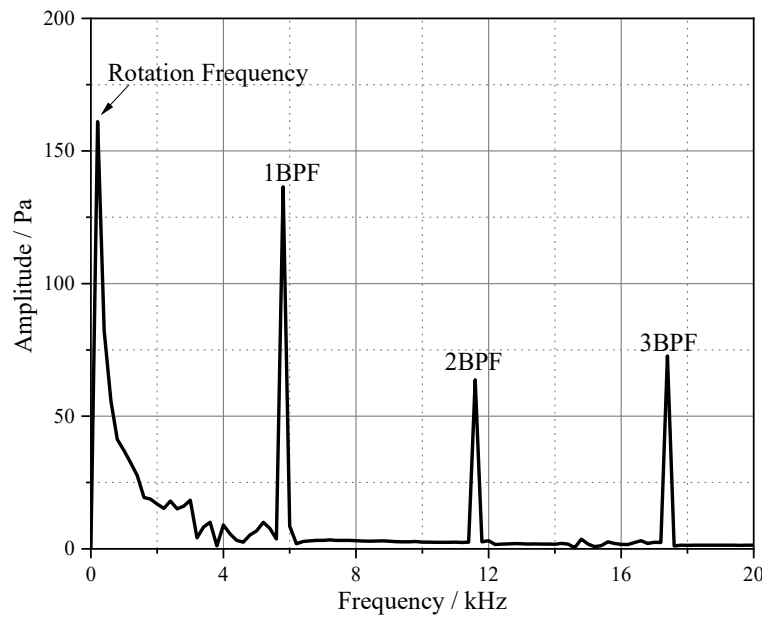


Figure 13. Pressure spectrum in front of LE under zero clearance model.

3.3. Detail Results of Design Clearance Model

Figure 14 delineates distribution of the time-averaged axial momentum of tip leakage flow. MD represents the condition at which the flow rate is intermediate between PE and NS. μ is defined as follows:

$$\mu = \int_{r_{tip}}^{r_{casing}} \frac{\rho V_n V_t}{\dot{m}_{in} V_z / c_x} dr \quad (7)$$

where \dot{m}_{in} is mass flow rate at rotor passage inlet, c_x is chord length of blade, subscript n is normal direction, t is tangent direction, z is axial direction.

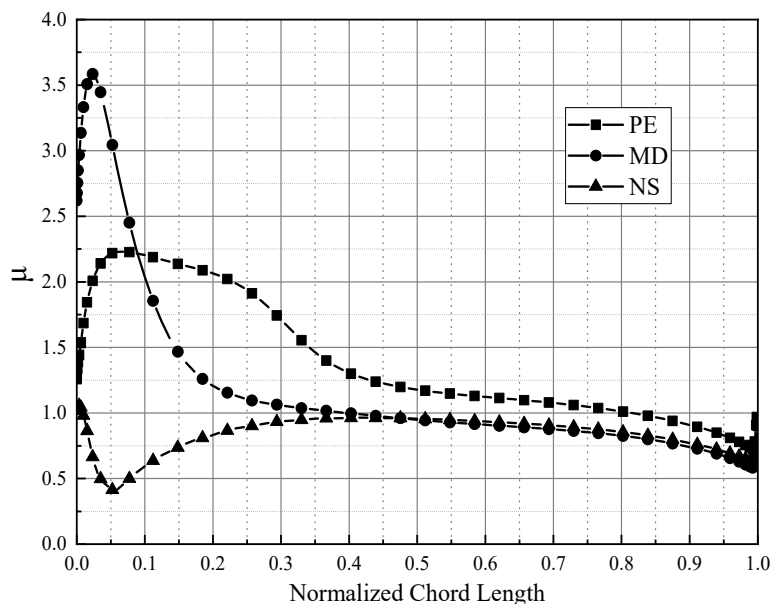


Figure 14. Momentum distribution of tip clearance flow along chord.

From this distribution, the axial momentum is concentrated at the front part of the chord. As the flow rate decreases, the centroid of μ moves to the leading edge, hence, the leakage flow in the rear of the clearance is smaller. The effect of the existence and the distribution of leakage flow will be discussed in following paragraphs.

Figure 15 shows contours of the Mach number and entropy at 99.35% of span. In general, with the influence of the tip leakage flow, flow field in the tip region is much different with the zero-clearance model. From Mach contours, in both PE and NS conditions, flow separation and serious blockage are suppressed at the suction side, which is the result in mixing with circumferential leakage flow. However, in the NS condition, there is a block of a low speed region along the pressure side, which is due to the tip clearance vortex. The leading-edge spillage also occurred, but the reason is not the leading-edge separation, but the TCV. From entropy contours, the high-gradient interface has moved to the rotor inlet. Hence, the main flow could not flow pass the passage, which caused the low speed region. However, with the circumferential flow from the tip clearance, the low speed region will not develop to a large blockage. When it is at a rear part of the passage, the low speed region could cross the passage and expand to the suction side. This is because the tip leakage flow in the rear part of the clearance is too small to supply enough momentum for a low speed region. As the flow in the tip region is dominated by the tip clearance vortex and tip leakage flow, from the streamlines at the passage outlet in Figure 16, in the rear part of clearance, there is the vortex generated by the sheared tip leakage flow.

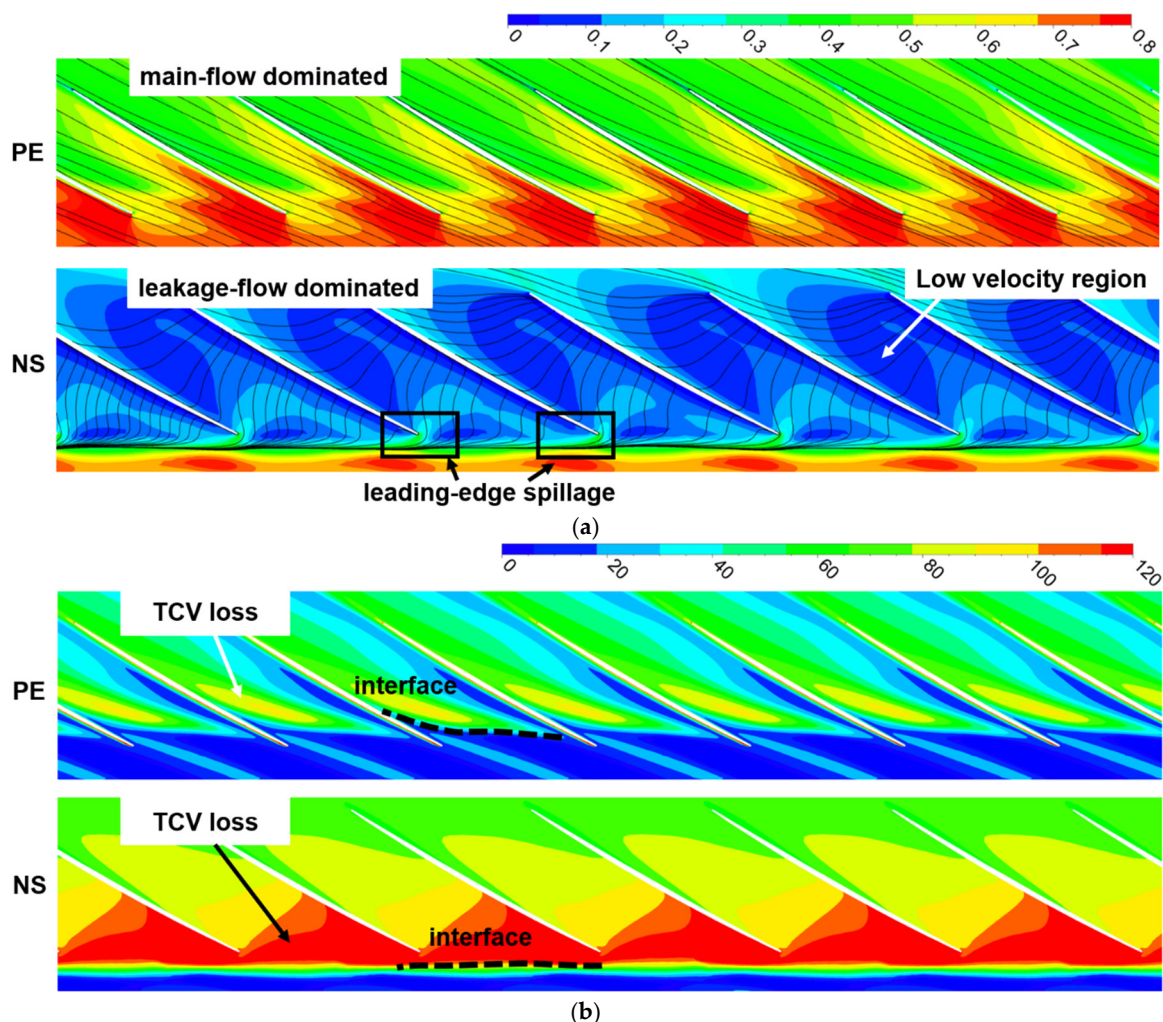


Figure 15. Time-averaged results at 96% of span. (a): Relative Mach contours with streamline of relative velocity. (b): Entropy contours ($\text{J}/(\text{kg K})$).

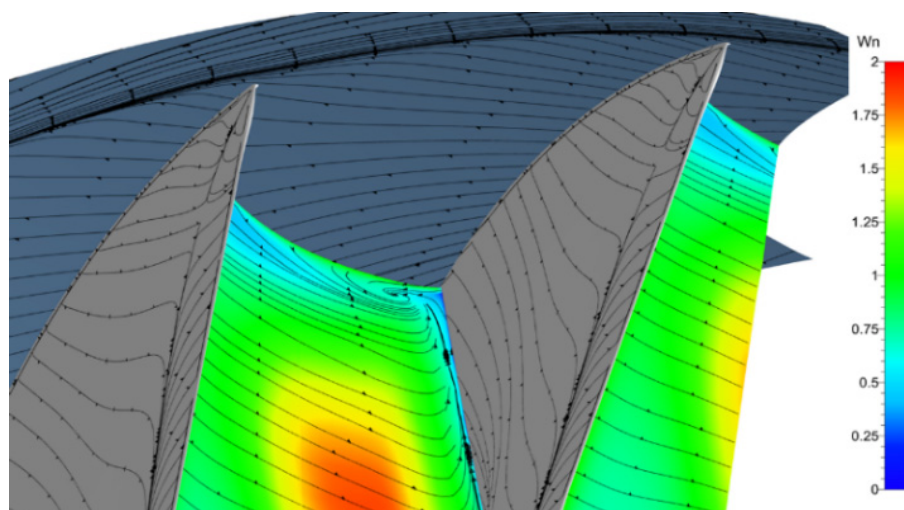


Figure 16. Streamline on suction side, casing, and passage outlet.

Figure 17 shows the axial component of the velocity, which can represent the location of the clearance vortex. P_{TCV} is a period of the shedding of the tip clearance vortex, which corresponds to about 0.5 Blade passing frequency (BPF). The tip clearance vortex results in the leading-edge spillage and mixing process between the main flow and tip leakage flow. Tip clearance vortex is formed near the leading edge, developed along the rotor passage inlet, interacted with the leading edge of the other side, and reduced along the pressure side. Streamlines from the tip clearance are shown in Figure 18, which can show the detail of the tip clearance vortex. Streamlines from the tip clearance roll up to a vortex, which is the result in the mixing process, with main flow near the leading edge. As the axial momentum ratio between the leakage flow and main flow increases, the vortex trajectory moves to the rotor inlet. When the streamlines reach the next leading edge, they are diverged. Some streamlines cross in front of the leading edge to the next passage, which is called leading-edge spillage. Streamline in the core of the vortex is developed and finally stagnated. Then the vortex breakdown occurs (as yellow blank locates), because the flow is a counter-pressure along the vortex trajectory. It can trigger several low speed cells (as the red dot line shows); some of them will be developed to become larger at the mid-passage. The streamlines near the large low-velocity cell begin to diverge by the blockage effect of low-velocity cells, which is called secondary vortex as black arrow shows. Moreover, when the larger low-velocity cell is developed near the next leading edge, the spillage streamlines will be increased by the blockage effect.

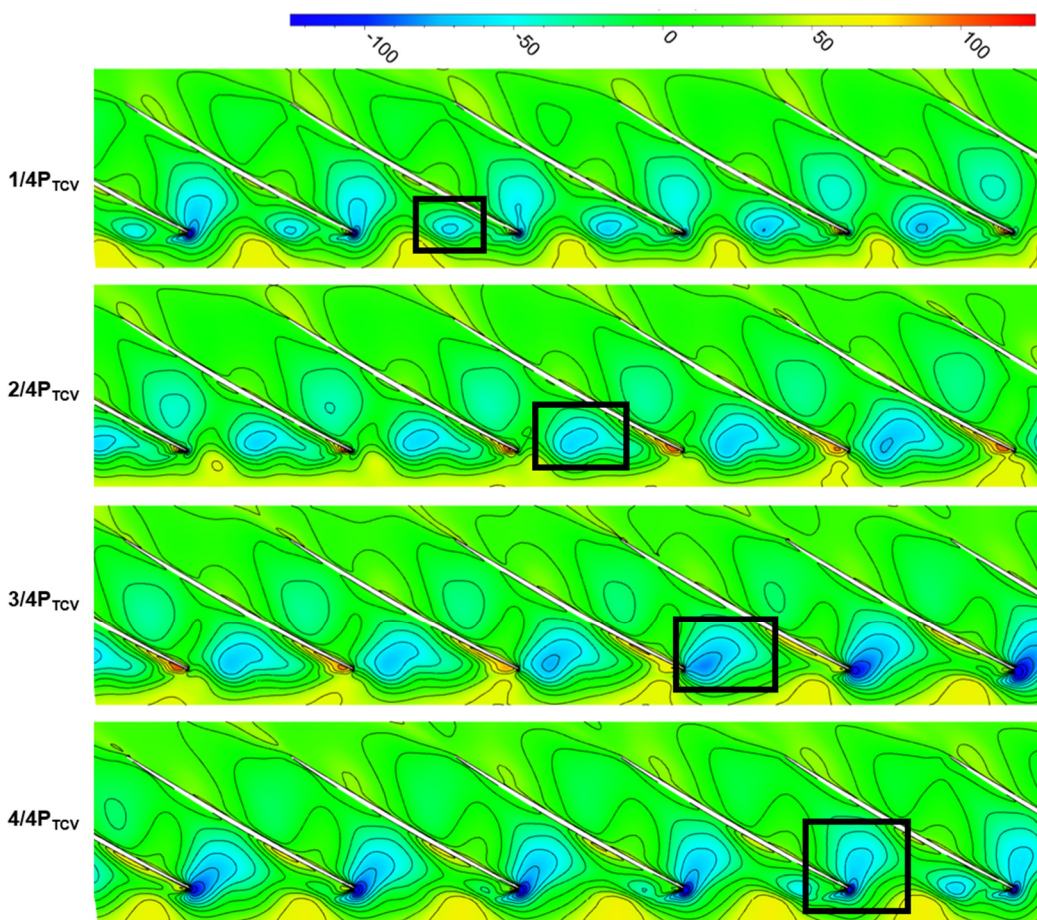


Figure 17. Unsteady contours of axial component of velocity. (P_{TCV} is the period of the TCV (tip clearance vortex) shedding).

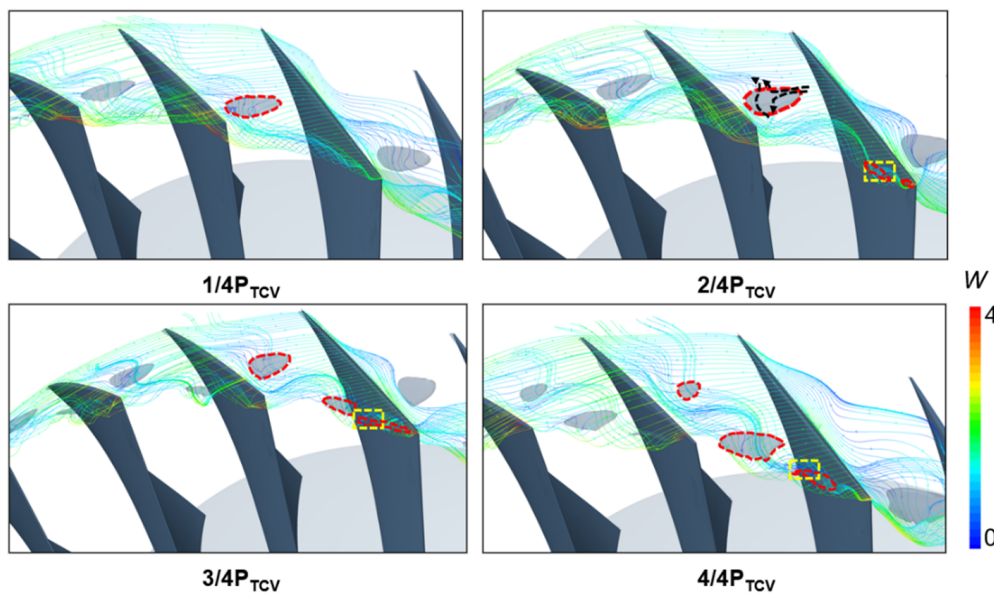


Figure 18. Unsteady streamlines from tip clearance with the iso-surface of $\text{Ma}_r = 0.2$, P_{TCV} is the period of the TCV (tip clearance vortex) shedding.

In addition, the unsteadiness in the tip region is enhanced (a lot) by vortex breakdown and secondary vortex, which is illustrated in Figure 19. Compared with the spectrum in PE and NS condition, the amplitude increase at BPFs are limited. However, the amplitudes at the frequencies related to the tip clearance vortex and rotation are increased from nearly zero. Compared with the spectrum of zero-clearance model in the NS condition, amplitude at BPFs are increased, while amplitudes at rotation frequencies are about the same.

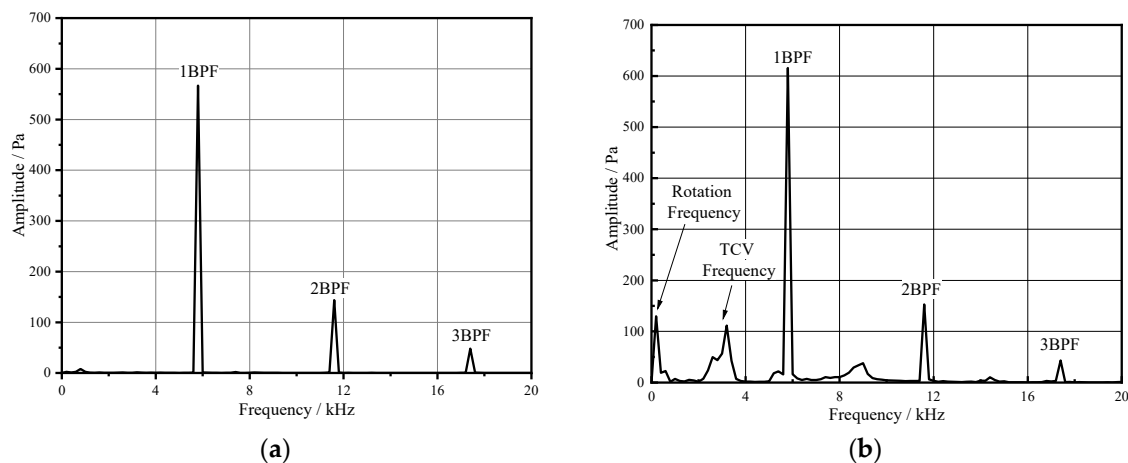


Figure 19. Pressure spectrum in front of LE under design clearance model. (a): under PE condition. (b): under NS condition.

To sum up, under design clearance model, the influence of tip clearance dominates flow field in the tip region. The separation at leading edge and casing-suction can be eliminated by the tip leakage flow. However, the low-velocity region can be triggered by the tip clearance vortex in NS condition. Moreover, the unsteadiness in the tip region is enhanced by the evolution of the tip vortex.

3.4. Detailed Results of Large Clearance Model

As the clearance is increased, the total leakage flow is increased correspondingly. From the Mach number in Figure 20a, the separation in the tip region is inhibited furtherly. However, as the tip leakage flow is increased in scale and value, flow structure in the tip region will be influenced, and the loss is increased with the tip clearance in Figure 20b. On the one hand, the radial scale of leakage flow is increased, which will enlarge the scale of the tip clearance vortex. On the other hand, the axial momentum ratio between leakage flow and main flow is increased, which is the reason for the forward-moving of the tip clearance vortex. Therefore, compared with design clearance, the forward spillage occurred in a larger flow rate. In addition, the low-velocity cell can only be developed to the front-middle passage, then its velocity will increase by the increased circumferential leakage flow. The unsteadiness in the tip region is also enhanced by the increasing of the tip clearance, which is illustrated by the moving of the low-velocity cell in Figure 21. As the spectrum shows in Figure 22, compared with that from the zero-clearance and design-clearance models, the amplitude at BPFs increased a lot.

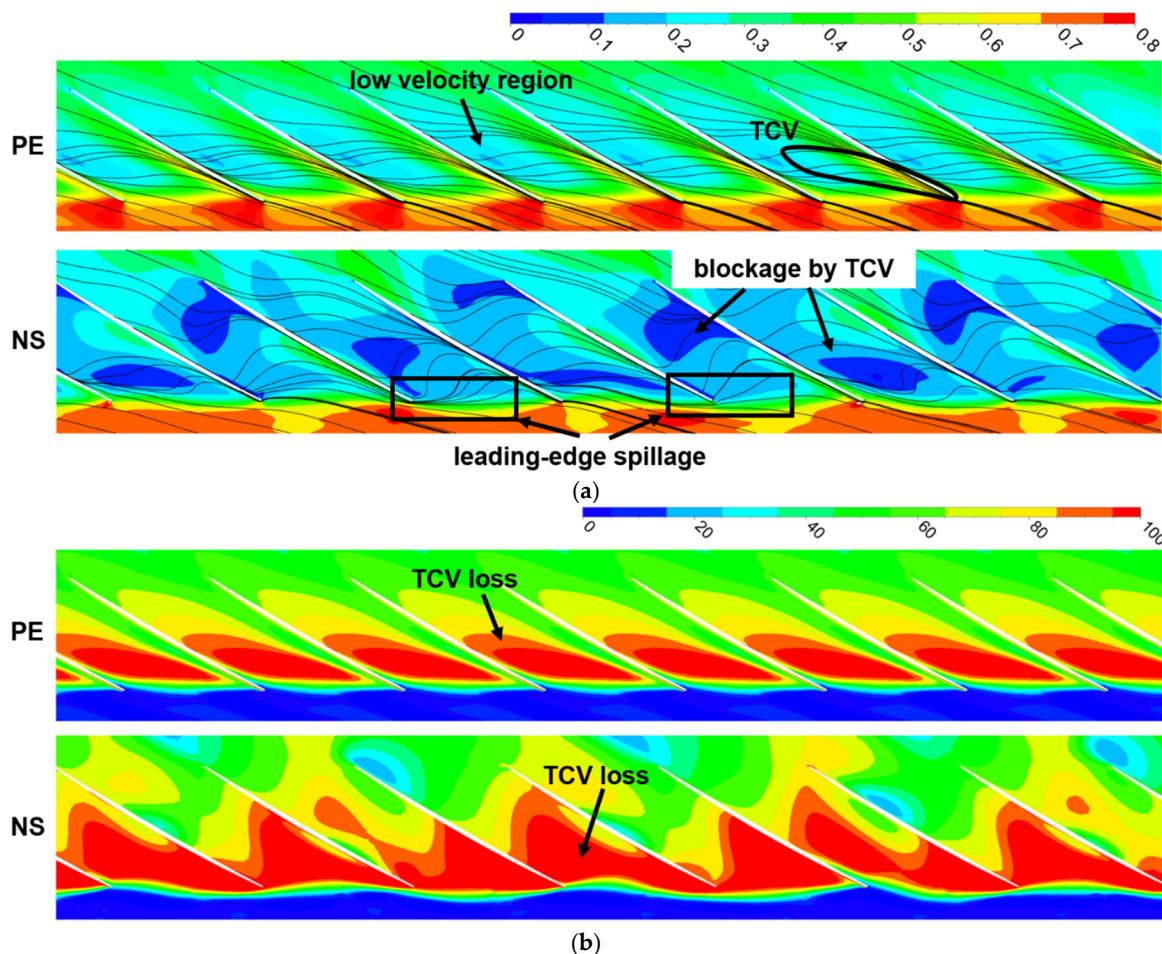


Figure 20. Time-averaged results at 96% of span. (a): Relative Mach contours with streamline of relative velocity. (b): Entropy contours ($\text{J}/(\text{kg K})$).

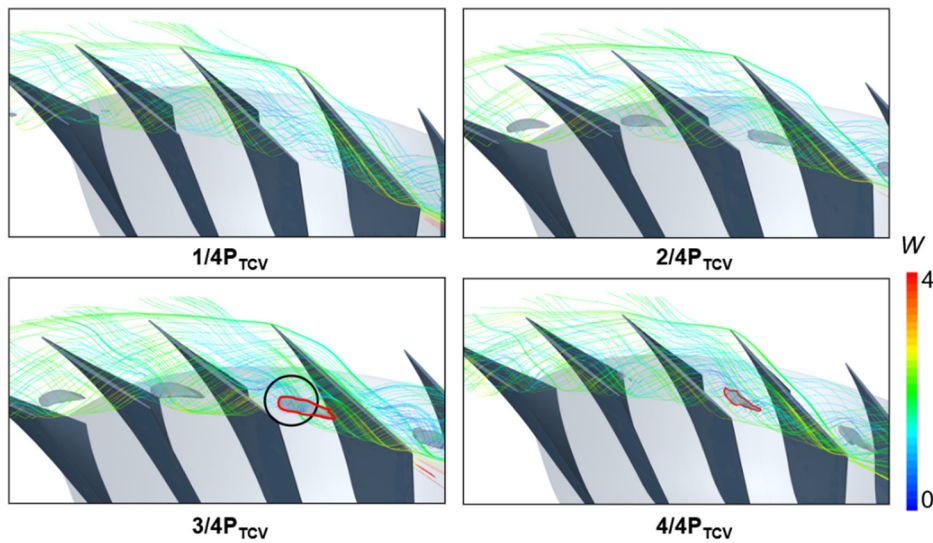


Figure 21. Unsteady streamlines from tip clearance with the iso-surface of $Ma_r = 0.2$, P_{TCV} is the period of the TCV (tip clearance vortex) shedding.

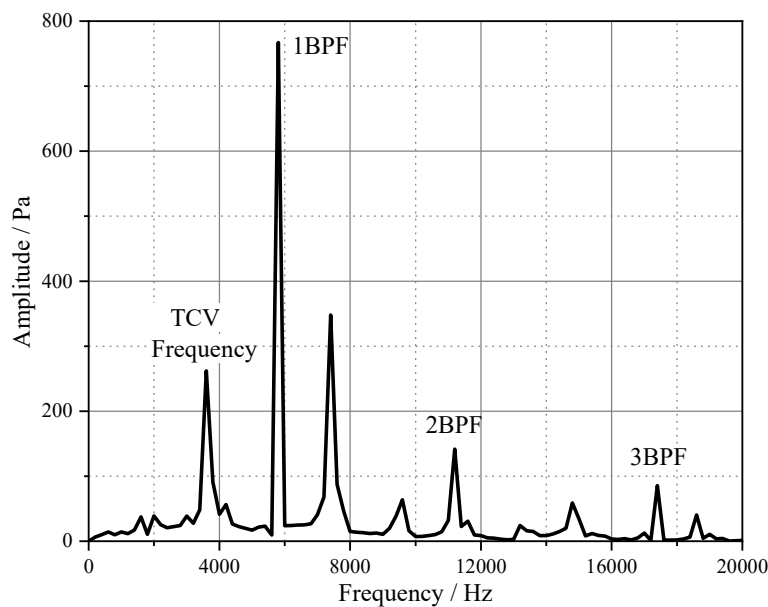


Figure 22. Pressure spectrum in front of LE under large clearance model.

4. Conclusions

This paper studies the influence of tip clearance on flow characteristics related to performance. Based on full-passage grids, the validated results are obtained by the means of the RANS method. A series of performance curves are obtained in different clearance models, from which it is found there exists an optimum clearance for a stable working range. It is found that the tip leakage flow can benefit the stable working range if the tip clearance is small enough, while it turns out to be harmful to the stability if the tip clearance is too large.

Under the zero clearance model, it is the separation at the casing-suction corner that dominates the flow field in the tip region. Under this blockage, incidence of upstream is increased, which will trigger larger separation in the next passage. Finally, some passages are fully blocked and stall occurs. As the tip clearance is increased from zero to the optimum value, the separation and blockage along the suction side are suppressed by tip leakage flow.

Under the design clearance model, the influence of the tip clearance dominates flow field in the tip region. The existence of the tip leakage flow can benefit to the reduction of separation at the leading edge and casing-suction. However, the low-velocity region can be triggered by the tip clearance vortex in NS condition. Moreover, the unsteadiness in the tip region is enhanced by the evolution of the tip vortex.

When the tip clearance increases to extent the tip leakage flow increases in scale and value. Therefore, the scale and unsteadiness of the tip clearance vortex increases correspondingly, which can trigger the forward spillage earlier.

Author Contributions: Conceptualization, M.S. and B.Y.; methodology, M.S.; software, M.S.; validation, M.S.; formal analysis, M.S.; investigation, M.S.; resources, B.Y.; data curation, M.S.; writing—original draft preparation, M.S.; writing—review and editing, H.X., B.Y.; and S.Z.; visualization, M.S.; supervision, B.Y.; project administration, B.Y.; funding acquisition, B.Y. All authors have read and agreed to the published version of the manuscript.

Funding: This research was funded by the National Science and Technology Major Project (2017-II-0006-0019).

Conflicts of Interest: The authors declare no conflict of interest.

Nomenclature

c	chord length at rotor tip
m	mass flow rate
P	pressure
v	velocity
w	relative velocity
T	Time
U	tangential velocity
V	absolute velocity projection to the span
W	relative velocity projection to the span

Greek Symbols

ρ	density
φ	normalized mass flow
π	total pressure ratio
τ	radial length of the tip clearance
ξ	isentropic efficiency

Abbreviations

BPF	blade passing frequency
CFD	computational fluid dynamics
IGV	inlet guide vane
DP	design condition
LE	leading edge
Ma	Mach number
NS	near stall condition
PE	peak efficiency condition
PS	pressure side
R1	rotor
S1	stator
SS	suction side
TCV	tip clearance vortex
TE	trailing edge
TLF	tip leakage flow

Subscript

i	inlet
o	outlet
r	relative
s	static variable
t	total variable
BPF	quantity related to the period of blade passing
TCV	quantity related to the period of the generation of tip clearance vortex

References

1. Lakshminarayana, B. Methods of predicting the tip clearance effects in axial flow turbomachinery. *J. Basic Eng.* **1970**, *92*, 467–480. [[CrossRef](#)]
2. Inoue, M.; Kuroumaru, M.; Fukuhara, M. Behavior of tip leakage flow behind an axial compressor rotor. *J. Eng. Gas Turbines Power* **1986**, *108*, 7–14. [[CrossRef](#)]
3. Inoue, M.M.; Kuroumaru, M.M. Structure of tip clearance flow in an isolated axial compressor rotor. *J. Turbomach.* **1989**, *111*, 250–256. [[CrossRef](#)]
4. Day, I.J. Stall inception in axial flow compressors. *J. Turbomach.* **1991**, *115*, 1–9. [[CrossRef](#)]
5. Khalid, S.A.; Khalsa, A.S.; Waitz, I.A.; Tan, C.S.; Greitzer, E.M.; Cumpsty, N.A.; Adamczyk, J.; Marble, F.E. Endwall blockage in axial compressors. *J. Turbomach.* **1999**, *121*, 499–509. [[CrossRef](#)]
6. Mailach, R.; Lehmann, I.; Vogeler, K. Rotating instabilities in an axial compressor originating from the fluctuating blade tip vortex. *J. Turbomach.* **2001**, *123*, 453–460. [[CrossRef](#)]
7. Mailach, R.; Sauer, H.; Vogeler, K. The periodical interaction of the tip clearance flow in the blade rows of axial compressors. In *ASME Turbo Expo 2001: Power for Land, Sea, and Air*; American Society of Mechanical Engineers: New York, NY, USA, 2001; p. V001T03A004. [[CrossRef](#)]
8. Sirakov, B.T.; Tan, C.S. Effect of unsteady stator wake—Rotor double-leakage tip clearance flow interaction on time-average compressor performance. *J. Turbomach.* **2003**, *125*, 465–474. [[CrossRef](#)]
9. Du, H.; Yu, X.; Liu, B. Modeling of the double leakage and leakage spillage flows in axial flow compressors. *J. Therm. Sci.* **2014**, *23*, 103–113. [[CrossRef](#)]
10. Hah, C. Effects of double-leakage tip clearance flow on the performance of a compressor stage with a large rotor tip gap. *J. Turbomach.* **2017**, *139*, 061006. [[CrossRef](#)]
11. Schlechtriem, S.; Lötzerich, M. Breakdown of tip leakage vortices in compressors at flow conditions close to stall. In *ASME 1997 International Gas Turbine and Aeroengine Congress and Exhibition*; American Society of Mechanical Engineers: New York, NY, USA, 1997; p. V001T03A004. [[CrossRef](#)]
12. Furukawa, M.; Saiki, K.; Nagayoshi, K.; Kuroumaru, M.; Inoue, M. Effects of stream surface inclination on tip leakage flow fields in compressor rotors. *J. Turbomach.* **1998**, *120*, 683–692. [[CrossRef](#)]
13. Furukawa, M.; Inoue, M.; Saiki, K.; Yamada, K. The role of tip leakage vortex breakdown in compressor rotor aerodynamics. In *ASME 1998 International Gas Turbine and Aeroengine Congress and Exhibition*; American Society of Mechanical Engineers: New York, NY, USA, 1998; p. V001T01A054. [[CrossRef](#)]
14. Furukawa, M.; Saiki, K.; Yamada, K.; Inoue, M. Unsteady flow behavior due to breakdown of tip leakage vortex in an axial compressor rotor at near-stall condition. In *ASME Turbo Expo 2000: Power for Land, Sea, and Air*; American Society of Mechanical Engineers: New York, NY, USA, 2000; p. V001T03A112. [[CrossRef](#)]
15. Yamada, K.; Funazaki, K.; Furukawa, M. The behavior of tip clearance flow at near-stall condition in a transonic axial compressor rotor. In *ASME Turbo Expo 2007: Power for Land, Sea, and Air*; American Society of Mechanical Engineers: New York, NY, USA, 2007; pp. 295–306. [[CrossRef](#)]
16. McDougall, N.M.; Cumpsty, N.A.; Hynes, T.P. Stall inception in axial compressors. *J. Turbomach.* **1990**, *112*, 116–123. [[CrossRef](#)]
17. McDougall, N.M. A comparison between the design point and near stall performance of an axial compressor. In *ASME 1989 International Gas Turbine and Aeroengine Congress and Exposition*; American Society of Mechanical Engineers: New York, NY, USA, 1989; p. V001T01A040. [[CrossRef](#)]
18. Camp, T.R.; Day, I.J. A Study of Spike and Modal Stall Phenomena in a Low-Speed Axial Compressor. *J. Turbomach.* **1998**, *120*, 393–401. [[CrossRef](#)]
19. Hoying, D.A.; Tan, C.S.; Vo, H.D.; Greitzer, E.M. Role of blade passage flow structures in axial compressor rotating stall inception. In *ASME 1998 International Gas Turbine and Aeroengine Congress and Exhibition*; American Society of Mechanical Engineers: New York, NY, USA, 1998; p. V001T01A138. [[CrossRef](#)]
20. Hah, C.; Bergner, J.; Schiffer, H.P. Short length-scale rotating stall inception in a transonic axial compressor: Criteria and mechanisms. In *ASME Turbo Expo 2006: Power for Land, Sea, and Air*; American Society of Mechanical Engineers: New York, NY, USA, 2006; pp. 61–70. [[CrossRef](#)]
21. Vo, H.D.; Tan, C.S.; Greitzer, E.M. Criteria for spike initiated rotating stall. *J. Turbomach.* **2008**, *130*, 011023. [[CrossRef](#)]
22. Pullan, G.; Young, A.M.; Day, I.J.; Greitzer, E.M.; Spakovszky, Z.S. Origins and structure of spike-type rotating stall. *J. Turbomach.* **2015**, *137*, 051007. [[CrossRef](#)]

23. Hewkin-Smith, M.; Pullan, G.; Grimshaw, S.D.; Greitzer, E.M.; Spakovszky, Z.S. The Role of Tip Leakage Flow in Spike-Type Rotating Stall Inception. In *ASME Turbo Expo 2017: Turbomachinery Technical Conference and Exposition*; American Society of Mechanical Engineers: New York, NY, USA, 2017; p. V02DT46A009. [[CrossRef](#)]
24. Spalart, P.; Allmaras, S. A one-equation turbulence model for aerodynamic flows. In Proceedings of the 30th Aerospace Sciences Meeting and Exhibit, Reno, NV, USA, 6–9 January 1992; p. 439.
25. Song, M.R.; Yang, B.; Dong, G.M.; Liu, X.L.; Wang, J.Q.; Xie, H.; Lu, Z.H. Research on Accuracy of Flowing Field Based on Numerical Simulation for Tonal Noise Prediction in Axial Compressor. In *ASME Turbo Expo 2018: Turbomachinery Technical Conference and Exposition*; American Society of Mechanical Engineers: New York, NY, USA, 2018; p. V02BT43A006.
26. Jameson, A. Time dependent calculations using multigrid, with applications to unsteady flows past airfoils and wings. In Proceedings of the 10th Computational Fluid Dynamics Conference, Honolulu, HI, USA, 24–26 June 1991; p. 1596.
27. Rai, M.M. Three-dimensional Navier-Stokes simulations of turbine rotor-stator interaction. Part I-Methodology. *J. Propuls. Power* **1989**, *5*, 305–311. [[CrossRef](#)]

Publisher's Note: MDPI stays neutral with regard to jurisdictional claims in published maps and institutional affiliations.



© 2020 by the authors. Licensee MDPI, Basel, Switzerland. This article is an open access article distributed under the terms and conditions of the Creative Commons Attribution (CC BY) license (<http://creativecommons.org/licenses/by/4.0/>).